

# Autonomous Distributed Angles-Only Navigation and Timekeeping in Lunar Orbit

Keidai Iiyama, Justin Kruger, Simone D’Amico, *Stanford University*

## BIOGRAPHY

**Keidai Iiyama** is a Ph.D. student in the Department of Aeronautics and Astronautics at Stanford University. He received his M.E. degree in Aerospace Engineering in 2021 from the University of Tokyo, where he also received his B.E. in 2019.

**Justin Kruger** is a Ph.D. candidate in the Department of Aeronautics and Astronautics at Stanford University. He received an M.S. degree from Stanford University (2019) and B.E. and B.S. degrees from the University of Western Australia (2016).

**Simone D’Amico** is Associate Professor of Aeronautics and Astronautics at Stanford University and W. M. Keck Faculty Scholar in the School of Engineering. He received the B.S. and M.S. degrees from Politecnico di Milano (2003) and the Ph.D. degree from Delft University of Technology (2010).

## ABSTRACT

This paper demonstrates an algorithmic framework for autonomous, distributed navigation and timekeeping for spacecraft swarms and constellations using angles-only measurements from onboard cameras. Angles-only methods are compelling as they reduce reliance on external measurement sources. However, prior flight demonstrations have faced limitations, including 1) inability to treat multi-agent space systems including multiple observers and targets in an accurate and timely manner, 2) lack of autonomy and reliance on external state information, and 3) treatment of primarily Earth-orbiting scenarios. The Absolute and Relative Trajectory Measurement System (ARTMS) discussed in this paper overcomes these challenges to enable future lunar missions. It consists of three novel algorithms: 1) Image Processing, which tracks and identifies targets in images and computes their bearing angles; 2) Batch Orbit Determination, which computes a swarm state initialization from angles-only measurements; and 3) Sequential Orbit Determination, which uses an unscented Kalman filter to refine the swarm state, seamlessly fusing measurements from multiple observers to achieve the necessary robustness and autonomy. This paper augments ARTMS for lunar navigation and its theoretical performance is investigated through a quantitative observability analysis. High-fidelity simulations with a star tracker in the loop demonstrate successful navigation of swarms and constellations in low lunar orbits, near-rectilinear halo orbits, and elliptic frozen orbits. ARTMS achieves absolute orbit estimation for all swarm members using only inter-satellite angles with simultaneous estimation of differential clock offsets and ballistic coefficients. It therefore presents an important capability for the support of future lunar and planetary exploration.

## I. INTRODUCTION

There is growing interest in establishing a sustainable human presence on the Moon via future manned and robotic missions [1]. Critical to the success of these efforts is the deployment of multiple spacecraft, including swarms and constellations, in cislunar and lunar space. For example, the NASA Goddard Space Flight Center has proposed the LunaNet concept, an extensible networked architecture for lunar communication and navigation [2]. Similarly, the ESA Moonlight concept proposes a dedicated lunar telecommunications and navigation constellation [3]. Additionally, the NASA Starling program has suggested applying swarms of autonomous satellites for lunar remote sensing and monitoring of Deep Space Gateway operations [4].

Currently, navigation in deep space and in lunar environments relies on regular radio contact with ground stations such as NASA’s Deep Space Network (DSN). This is neither optimal nor practical in the long term because dedicated ground stations are limited in number and will soon be oversubscribed, preventing scalability to larger numbers of lunar spacecraft [5]. In addition, navigation delays are introduced by ground-in-the-loop elements, limiting the autonomy of space assets [6]. Radio navigation is also impacted on the far side of the Moon where direct communication with Earth ground stations is unavailable.

In response to these limitations, recent research has explored the challenges of receiving Earth-orbit Global Navigation Satellite System (GNSS) signals at lunar distances. Key technologies are high-gain GNSS receivers to track weak sidelobe signals and efficient filtering algorithms to mitigate dilution of precision due to poor variation in line-of-sight (LOS) vectors to GNSS satellites. Simulations have demonstrated the use of Global Positioning System (GPS) sidelobe signals for positioning, navigation, and timing in various lunar orbits, including moon transfer orbits [7][8], Elliptic Lunar Frozen Orbits (ELFOs) [9], and Near-Rectilinear Halo Orbits (NRHOs) [10] [11]. Several flight missions are scheduled to test these capabilities including NASA’s Lunar GNSS Receiver Experiment [12] and ESA’s Lunar Pathfinder [13].

An alternative approach for navigation of multi-agent space systems is optical angles-only navigation, whereby star trackers or other vision-based sensors (VBS) aboard observer satellites in the swarm or constellation provide bearing angle measurements to target resident space objects (RSO). This overcomes several drawbacks of GNSS-based navigation, in that 1) a dedicated high-gain GNSS receiver is not required, 2) tracking can also be performed for unknown or uncooperative targets, and 3) navigation is not affected by occultation on the far side of the Moon or other GNSS signal dropouts. Cameras are passive, robust, low size-weight-power-cost sensors with high dynamic range that are already present on the majority of spacecraft. They may obtain measurements of non-cooperative targets such as space debris or satellites without active sensors, and reliance on external measurement sources is reduced or eliminated.

Two prior flight experiments have demonstrated angles-only navigation in orbit. In 2012, the Advanced Rendezvous using GPS and Optical Navigation (ARGON) experiment enabled the rendezvous of two smallsats in Low Earth Orbit (LEO) from inter-satellite separations of 30 km to 3 km [14]. This was followed by the Autonomous Vision Approach Navigation and Target Identification (AVANTI) experiment in 2016, which similarly conducted a rendezvous of two smallsats from separations of 13 km to 50 m [15]. Although these demonstrations were successful, they are characterized by four key deficiencies: 1) inability to accommodate multiple observers and multiple targets 2) reliance on accurate a-priori relative orbit information for initialization, 3) reliance on external knowledge of the observer's absolute orbit to maintain state convergence, and 4) reliance on frequent translational maneuvers to resolve the weakly observable target range.

To overcome these deficiencies and enable future distributed missions in deep space, Stanford's Space Rendezvous Laboratory (SLAB) has proposed the Absolute and Relative Trajectory Measurement System (ARTMS) [16] [17]. ARTMS is an autonomous Angles-only navigation architecture for multi-agent space systems divided into three modules and corresponding new algorithms: Image Processing (IMP) [18], Batch Orbit Determination (BOD) [19], and Sequential Orbit Determination (SOD) [16]. IMP identifies multiple RSOs in 2D images from a single monocular camera without requiring a-priori relative orbit knowledge. BOD generates an initial state estimate for all participating satellites by using batches of angles to targets and a single coarse absolute orbit initialization for the observer. SOD continually refines the ARTMS state estimate using a newly designed unscented Kalman filter (UKF), fusing measurements from multiple observers broadcast over an inter-satellite link (ISL) to achieve complete state observability and time synchronization. In this fashion, ARTMS enables distributed, autonomous, and scalable angles-only navigation with minimal reliance on external or a-priori information and no reliance on maneuvers.

ARTMS is due to be flight-tested in LEO during the upcoming the Starling Formation-flying Optical eXperiment (StarFOX) [4]. StarFOX is one of the primary payloads of NASA Starling, a four-CubeSat technology demonstration mission scheduled for launch in 2022. Its applicability to deep space has been studied as part of a collaboration between SLAB and the NASA Jet Propulsion Laboratory, which successfully demonstrated robust navigation across a variety of formations in Mars orbit through a quantitative observability analysis and camera-in-the-loop simulations [20].

This paper extends and examines the applicability of ARTMS for navigation and timekeeping in lunar space. New challenges must be addressed because the lunar dynamic environment is substantially different from Earth or Mars due to a weaker central gravitational potential, significant gravitational anomalies, and comparatively stronger third-body and solar radiation pressure (SRP) perturbations. Many lunar orbits are therefore unstable, and choices for stable orbits such as NRHO are highly elliptical with long orbit periods. This poses challenges on the weaker observability of angles-only navigation and ARTMS algorithms must be augmented for navigation in slow-moving and highly-perturbed scenarios. Envisioned distributed space systems around the Moon can also be characterized by large separations, i.e. constellations rather than swarms, which may impact target optical visibility and the accuracy of linearizations within ARTMS. Third, the frequency of Earth ground contacts for spacecraft clock resets/initialization will likely be low, requiring robust long-term timekeeping throughout the swarm or constellation.

In this work, ARTMS is extended with several algorithmic developments, including 1) on-board estimation of differential clock offsets and ballistic coefficients for more autonomy and robustness, 2) revised internal dynamics models in both analytic and numeric forms for accurate, efficient state propagation in lunar orbits, and 3) new VBS target tracking modes for enhanced measurement availability in highly elliptical and constellation orbits. This is complemented by a quantitative observability analysis which examines theoretical navigation performance for low- and high-altitude orbits, near-circular and eccentric orbits, close-range in-train and passive safety ellipse formations, and a constellation. Analysis indicates that all proposed scenarios are observable, though particular challenges are faced for the NRHO and constellation cases discussed in the paper.

To validate the analysis, high-fidelity simulations of ARTMS navigation in lunar orbit are also conducted using an optical stimulator with star tracker hardware-in-the-loop (HIL). Despite challenging measurement conditions, suitable navigation accuracy and robustness is achieved for varying orbit regimes. ARTMS therefore demonstrates the capability of autonomous distributed angles-only navigation and timekeeping to enable and support future lunar exploration.

The paper is organized as follows. Section II presents the mathematical background of the ARTMS measurement model, dynamics model, and estimated state. Section III introduces the ARTMS architecture and the algorithms necessary to enable angles-only navigation in lunar orbit. Section IV presents the observability analysis. Section V details the simulated lunar missions and data generation pipeline, with the discussion of results. Section VI contains concluding remarks.

## II. MODELING PRELIMINARIES

### 1. Measurement Model

The ARTMS payload produces angles-only measurements by computing the time-tagged bearing angles to objects detected in VBS images. First, define the radial/along-track/cross-track (RTN) frame of the observer, denoted  $\mathcal{R}$ . It is centered on and rotates with the observer and consists of orthogonal basis vectors  $\hat{\mathbf{x}}^{\mathcal{R}}$  (directed along the observer's absolute position vector);  $\hat{\mathbf{z}}^{\mathcal{R}}$  (directed along the observer's orbital angular momentum vector); and  $\hat{\mathbf{y}}^{\mathcal{R}} = \hat{\mathbf{z}}^{\mathcal{R}} \times \hat{\mathbf{x}}^{\mathcal{R}}$  [21]. Similarly, define a frame  $\mathcal{W}$  using  $\hat{\mathbf{y}}^{\mathcal{W}}$  (directed along the observer's velocity vector);  $\hat{\mathbf{z}}^{\mathcal{W}} = \hat{\mathbf{z}}^{\mathcal{R}}$ ; and  $\hat{\mathbf{x}}^{\mathcal{W}} = \hat{\mathbf{y}}^{\mathcal{W}} \times \hat{\mathbf{z}}^{\mathcal{W}}$ .  $\mathcal{W}$  only differs from  $\mathcal{R}$  by a rotation of the observer flight path angle  $\phi_f$  about  $\hat{\mathbf{z}}^{\mathcal{R}}$  with  $\phi_f \approx 0$  in near-circular orbits [21]. Bearing angles consist of azimuth and elevation  $(\alpha, \epsilon)$  and subtend the LOS vector  $\delta \mathbf{r}^{\mathcal{V}} = (\delta r_x^{\mathcal{V}}, \delta r_y^{\mathcal{V}}, \delta r_z^{\mathcal{V}})$  from the observer to the target. Superscript  $\mathcal{V}$  indicates description in the observer VBS coordinate frame, consisting of orthogonal basis vectors  $\hat{\mathbf{x}}^{\mathcal{V}}, \hat{\mathbf{y}}^{\mathcal{V}}, \hat{\mathbf{z}}^{\mathcal{V}}$ . The VBS may be aligned as necessary to keep swarm targets in the field of view (FOV). Bearing angles are then computed via [16].

$$\begin{pmatrix} \alpha \\ \epsilon \end{pmatrix}^{\mathcal{V}} = \begin{pmatrix} \arcsin \delta r_y^{\mathcal{V}} / \|\delta \mathbf{r}^{\mathcal{V}}\|_2 \\ \arctan \delta r_x^{\mathcal{V}} / \delta r_z^{\mathcal{V}} \end{pmatrix} \quad (1)$$

Bearing angles can be related to the inertial frame by rotating  $\delta \mathbf{r}^{\mathcal{V}}$  into the Moon-Centered Inertial (MCI) frame  $\mathcal{M}$ , as per

$$\delta \mathbf{r}^{\mathcal{M}} = {}^{\mathcal{V}}\vec{\mathbf{R}}^{\mathcal{M}} \delta \mathbf{r}^{\mathcal{V}} \quad (2)$$

where  ${}^{\mathcal{V}}\vec{\mathbf{R}}^{\mathcal{M}}$  denotes a rotation from frame  $\mathcal{V}$  into frame  $\mathcal{M}$ . This rotation matrix is computed by performing attitude determination using stars identified by the VBS [14]. Rotation matrices  ${}^{\mathcal{R}}\vec{\mathbf{R}}^{\mathcal{M}}$  and  ${}^{\mathcal{W}}\vec{\mathbf{R}}^{\mathcal{M}}$  can be computed using the observer's absolute orbit estimate. Figure 1 depicts the relationship between coordinate frames and bearing angles.

### 2. State Parametrization

ARTMS represents the absolute state  $\alpha$  of the observer in terms of quasi-nonsingular orbit elements (OE), with

$$\alpha = \begin{pmatrix} a \\ e_x \\ e_y \\ i \\ \Omega \\ u \end{pmatrix} = \begin{pmatrix} a \\ e \cos \omega \\ e \sin \omega \\ i \\ \Omega \\ \omega + M \end{pmatrix} \quad (3)$$

Above,  $a, e, i, \Omega, \omega$ , and  $M$  are the canonical Keplerian OE of semi-major axis, eccentricity, inclination, right ascension of the ascending node, argument of periapsis, and mean anomaly respectively, and  $u$  is the mean argument of latitude. All are computed with respect to  $\mathcal{M}$ . Fully nonsingular OE can be used for equatorial orbits [21].

The relative orbit  $\delta \alpha$  of a target spacecraft, as tracked by an observer, is described by the quasi-nonsingular relative orbit elements (ROE) [22]. The ROE state parametrization is defined in terms of the absolute OE of the observer and target (denoted by subscripts 'o' and 't' respectively) via

$$\delta \alpha = \begin{pmatrix} \delta a \\ \delta \lambda \\ \delta e_x \\ \delta e_y \\ \delta i_x \\ \delta i_y \end{pmatrix} = \begin{pmatrix} \delta a \\ \delta \lambda \\ |\delta e| \cos \phi \\ |\delta e| \sin \phi \\ |\delta i| \cos \theta \\ |\delta i| \sin \theta \end{pmatrix} = \begin{pmatrix} (a_t - a_o)/a_o \\ (u_t - u_o) + (\Omega_t - \Omega_o) \cos i_o \\ e_{x,t} - e_{x,o} \\ e_{y,t} - e_{y,o} \\ i_t - i_o \\ (\Omega_t - \Omega_o) \sin i_o \end{pmatrix} \quad (4)$$

Above,  $\delta a$  is the relative semi-major axis,  $\delta \lambda$  is the relative mean longitude,  $\delta e = (\delta e_x, \delta e_y)$  is the relative eccentricity vector with magnitude  $\delta e$  and phase  $\phi$ , and  $\delta i = (\delta i_x, \delta i_y)$  is the relative inclination vector with magnitude  $\delta i$  and phase  $\theta$ . Fully nonsingular ROE have also been defined for equatorial orbits [23].

The ARTMS state also includes several optional components. First are absolute empirical accelerations for the observer and

differential empirical accelerations for targets, defined as

$$\mathbf{a}_{\text{emp}}^{\mathcal{R}} = \begin{pmatrix} a_x \\ a_y \\ a_z \end{pmatrix}^{\mathcal{R}} \quad \delta \mathbf{a}_{\text{emp}}^{\mathcal{R}} = \begin{pmatrix} \delta a_x \\ \delta a_y \\ \delta a_z \end{pmatrix}^{\mathcal{R}} = \begin{pmatrix} a_{x,t} - a_{x,o} \\ a_{y,t} - a_{y,o} \\ a_{z,t} - a_{z,o} \end{pmatrix}^{\mathcal{R}} \quad (5)$$

respectively in  $\mathcal{R}$ . Empirical accelerations are used to approximately capture unmodeled dynamics, and are more computationally efficient than numerically integrating the full differential equations of relative motion [24]. Additional state components are the absolute clock errors and clock drift rates of the observer, and differential clock offsets and clock drift rates of targets with respect to the observer, defined as

$$\mathbf{c}_{\text{err}} = \begin{pmatrix} c_{\text{err}} \\ d_{\text{err}} \end{pmatrix} \quad \delta \mathbf{c}_{\text{err}} = \begin{pmatrix} \delta c_{\text{err}} \\ \delta d_{\text{err}} \end{pmatrix} = \begin{pmatrix} c_{\text{err},t} - c_{\text{err},o} \\ d_{\text{err},t} - d_{\text{err},o} \end{pmatrix} \quad (6)$$

Above,  $c_{\text{err}}$  is a clock offset and  $d_{\text{err}}$  is a clock drift rate. The absolute ballistic coefficient of the observer and differential ballistic coefficients of targets with respect to the observer can also be estimated, denoted as

$$\mathbf{B} = \begin{pmatrix} B_{\text{atm}} \\ B_{\text{srp}} \end{pmatrix} \quad \delta \mathbf{B} = \begin{pmatrix} \delta B_{\text{atm}} \\ \delta B_{\text{srp}} \end{pmatrix} = \begin{pmatrix} B_{\text{atm},t} - B_{\text{atm},o} \\ B_{\text{srp},t} - B_{\text{srp},o} \end{pmatrix} \quad (7)$$

For the lunar case, only the SRP coefficient is taken into account. Thus, for  $n$  detected targets, the complete ARTMS state is

$$\mathbf{x} = (\boldsymbol{\alpha}, \mathbf{a}, \mathbf{c}, \mathbf{B}, \delta \boldsymbol{\alpha}_1, \delta \mathbf{a}_1, \delta \mathbf{c}_1, \delta \mathbf{B}_1, \dots, \delta \boldsymbol{\alpha}_n, \delta \mathbf{a}_n, \delta \mathbf{c}_n, \delta \mathbf{B}_n) \quad (8)$$

Reasoning behind this choice of state parametrization is discussed in Section III.3.

### 3. Dynamics Model

ARTMS propagates the absolute orbits of observer and target spacecraft using fourth-order Runge-Kutta integration of the Gauss Variational Equations (GVE). For state  $\boldsymbol{\alpha}$ , the osculating OE of each spacecraft evolve according to

$$\dot{\boldsymbol{\alpha}} = G(\boldsymbol{\alpha}) \mathbf{d}^{\mathcal{R}} \quad (9)$$

where  $G \in \mathbf{R}^{6 \times 3}$  is the well-documented GVE state transition matrix [25] and  $\mathbf{d}^{\mathcal{R}}$  is the perturbing acceleration expressed in  $\mathcal{R}$ . Depending on the orbit regime, common perturbations are spherical harmonic gravity, atmospheric drag, third-body gravity and SRP. Analytic dynamics models for the mean OE which include the effects of  $J_2$ ,  $J_3$  and third-body gravitational perturbations are alternately used when computational efficiency is paramount.  $J_2$  causes secular drifts in  $M$ ,  $\omega$  and  $\Omega$  [26];  $J_3$  causes long-periodic changes in  $e$ ,  $i$ ,  $\omega$  and  $\Omega$  [27]; and third-body gravity causes double-averaged changes in  $e$ ,  $i$ ,  $\omega$  and  $\Omega$  [28]. Analytic linear models including  $J_2$ , differential drag and SRP are also available for ROE [23] [29].

A useful aspect of the ROE is that they provide geometric intuition regarding target relative motion. As shown in [22] for near-circular orbits, there is a linear map between the ROE and the target's curvilinear position vector  $\delta \mathbf{r}$  in the observer's RTN frame. The near-circular case was extended to eccentric orbits [24] by defining the eccentric ROE  $\delta \boldsymbol{\alpha}^* = (\delta a, \delta \lambda^*, \delta e_x^*, \delta e_y^*, \delta i_x, \delta i_y)$ . The eccentric ROE revert to traditional ROE for  $e_o \approx 0$ . The resulting map is

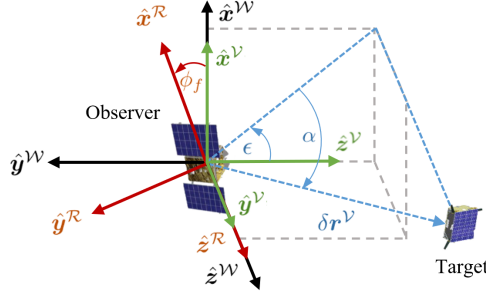
$$\delta \mathbf{r}^{\mathcal{R}} \approx r_o \begin{bmatrix} \delta a - \frac{e_o}{2} \delta e_x^* - \delta e^* \left( \cos(f_o - \phi^*) + \frac{e_o}{2} \cos(2f_o - \phi^*) \right) \\ \delta \lambda^* + \delta e^* \left( 2 \sin(f_o - \phi^*) + \frac{e_o}{2} \sin(2f_o - \phi^*) \right) \\ \delta i \sin(f_o + \omega_o - \theta) \end{bmatrix} \quad (10)$$

Figure 2 presents relative motion in RTN for small separations. Oscillatory motion produced by target relative orbits is shown in black, possessing the same frequency as the orbit. Oscillatory motion produced by orbit eccentricity is shown in red, acting at twice the frequency of the orbit.  $\delta a$  and  $\delta \lambda^*$  capture mean offsets in the radial and along-track directions respectively; magnitudes of  $\delta e^*$  and  $\delta i$  correspond to magnitudes of oscillations in the RT and RN planes respectively; and phases of  $\delta e^*$  and  $\delta i$  dictate the orientation and aspect ratio of the tilted ellipse in the RN plane. The eccentricity of the observer's orbit superimposes additional offsets and higher-frequency oscillations in the RT and RN planes.

Clock offsets are propagated within ARTMS using a random-walk process defined as

$$\dot{\mathbf{c}}_{\text{err}} = \begin{bmatrix} d_{\text{err}} \\ 0 \end{bmatrix} \quad (11)$$

where  $T_s$  is the propagation timestep. Spacecraft ballistic coefficients are modeled as constants within ARTMS.



**Figure 1:** Definition of target bearing angles with respect to  $\mathcal{V}$ ,  $\mathcal{R}$  and  $\mathcal{W}$ , with the VBS pointing in the anti-velocity direction.

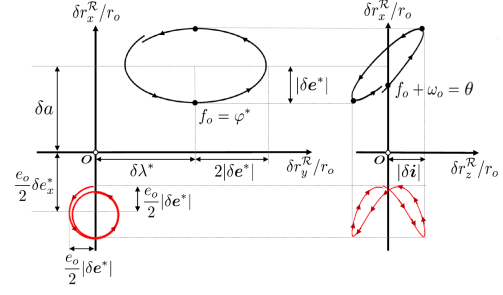


**Figure 2:** Target relative motion in the  $\hat{\mathbf{x}}^{\mathcal{R}}\text{-}\hat{\mathbf{y}}^{\mathcal{R}}$  (RT) and  $\hat{\mathbf{x}}^{\mathcal{R}}\text{-}\hat{\mathbf{z}}^{\mathcal{R}}$  (RN) planes. Motion that is first-order in spacecraft separation is in black. Contributions proportional to  $e$  are in red [16].

### III. ARTMS ARCHITECTURE

ARTMS is a self-contained software payload that provides autonomous, distributed angles-only navigation for spacecraft multi-agent space systems in planetary orbit regimes [16] [17] [20]. The following terminologies are adopted. ‘‘Observer’’ refers to the spacecraft hosting the instance of ARTMS being discussed. A ‘‘remote observer’’ is another spacecraft hosting an ARTMS payload that is providing measurements over the Inter-Satellite Link (ISL). The ‘‘swarm’’ consists of all observers and all other relevant ‘‘targets’’, which are space objects tracked by the observers. Observers might only track a subset of the swarm and targets may themselves be remote observers. Figure 3 presents an example (not to scale).

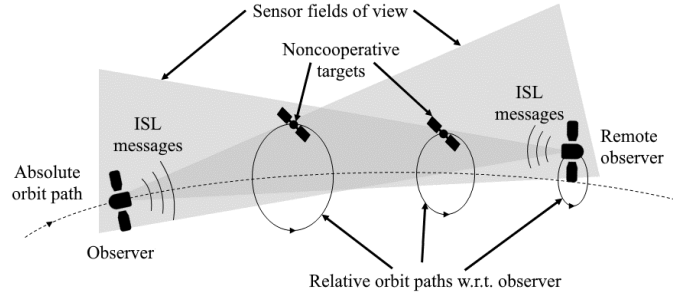


**Figure 3:** Illustration of ARTMS observers and targets. Not to scale.

A high-level overview of ARTMS is presented in Figure 4. It consists of three core software modules: IMage Processing (IMP), Batch Orbit Determination (BOD) and Sequential Orbit Determination (SOD). Data sources are the VBS, which provides time-tagged images to ARTMS; the ISL, which communicates orbit estimates and bearing angle measurements between swarm observers; the spacecraft bus, which provides additional attitude estimates if available; and the ground segment, which provides telecommands and receives telemetry. In this paper, it is assumed GNSS measurements are unavailable.

The operation of each module is briefly described as follows. First, the IMP module uses VBS images to produce batches of bearing angle measurements with corresponding uncertainties for all detected targets in the field of view (FOV). The only prior information needed by IMP is a coarse estimate of the observer’s absolute orbit at a single past epoch, provided by a source such as the DSN. Sample times for IMP image measurements are chosen as 0.5-2% of the orbit period. The BOD module uses IMP angle batches, as well as the aforementioned observer orbit estimate, to compute state estimates for the observer and its targets. BOD is run once per orbit. The SOD module uses the BOD estimate to initialize a UKF, which fuses measurements from IMP and remote observers to refine the state estimates of the observer and its targets. The resulting stereo bearing angle measurements greatly improve state estimate robustness, convergence, and accuracy. Subsequent BOD estimates are used for fault detection in SOD and re-initializations in contingency cases. SOD also provides updated state estimates to IMP to more

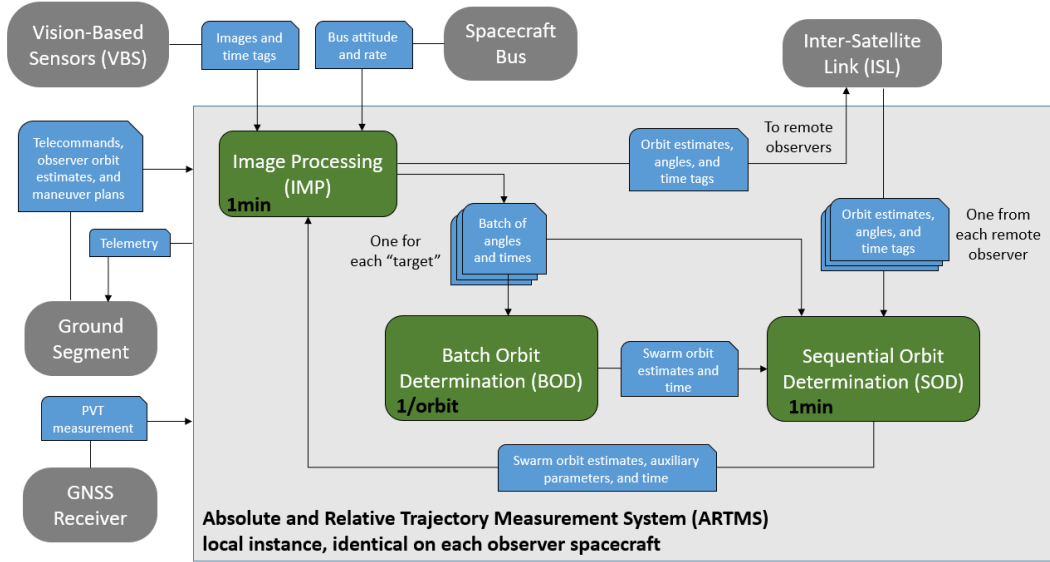


**Figure 4:** General architecture of ARTMS including external systems/data sources (dark gray), software modules (green), and exchanged data (blue). GNSS inputs (when available) and ground inputs are provided to all modules. Ground telemetry consists of all modules’ outputs.

efficiently assign new bearing angles to existing targets. The SOD orbit estimate and IMP bearing angles are sent to the ISL. All modules may utilize ground information when appropriate such as knowledge of planned swarm maneuvers. In this fashion, ARTMS is distributed across the swarm and is scalable to arbitrary swarm sizes. Furthermore, modules require almost no contact with ground-based resources. Novel algorithms self-initialize navigation using a single external absolute orbit measurement per observer and modules take advantage of additional information when available to enable near-total autonomy. The IMP [18], BOD [19] and SOD [16] algorithms are described in more detail in the following sections, along with extensions to ARTMS to enable navigation for general multi-agent space systems in lunar orbit.

## 1. Image Processing

The objective of IMP is to produce batches of time-tagged bearing angle measurements to each target using a coarse estimate of the observer’s orbit and images provided by the VBS.

First, a centroiding algorithm is used to simplify the image into a list of pixel cluster centroids [30]. Centroids are converted to unit vectors in the VBS frame using a calibrated camera model. Next, the Pyramid star identification algorithm [31] is applied to remove stellar objects (SO) from the list of vectors. Uncatalogued SO are detected as objects with unchanging inertial unit vectors between images and camera hotspots are detected as objects with unchanging pixel coordinates [15]. The VBS attitude is computed from the pointing vectors to identified stars in the inertial and sensor frames using the q-method [32]. The remaining minimal set of inertial unit vectors corresponds to potential targets and other unknown objects. If SOD is initialized, IMP uses the SOD state estimate to compute predicted target bearing angles and associated covariance regions, and applies the Mahalanobis distance between predictions and measurements to assign angles to existing targets. If no a-priori relative orbit knowledge is available, IMP employs the novel Spacecraft Angles-only MULTitarget tracking System (SAMUS) algorithm to detect target tracks in sets of unidentified measurements [18].

SAMUS applies concepts of multi-hypothesis tracking (MHT) [33] in that as measurements arrive, several simultaneous hypotheses are maintained for their association into target tracks. MHT robustly converges towards the correct hypothesis over time as more information becomes available gating, scoring, and pruning its propagated hypotheses. SAMUS achieves improved precision and efficiency compared to naive MHT by leveraging domain-specific knowledge to develop new kinematic scoring and trimming criteria. These criteria are derived from Equation 10 which maps OE and ROE to target relative position in  $\mathcal{R}$ . Note that true anomaly  $f_o$  is the only quickly-varying term whereas other terms, defined by the OE and ROE, vary slowly in the presence of perturbations such as third-body gravity and SRP [22]. These terms are effectively constant on the timescales of image-to-image tracking and target motion is therefore periodic with known form. Even if specific ROE are unknown, this kinematic model can be leveraged to assess target tracks formed by successive measured unit vectors in  $\mathcal{R}$ .

The radial and cross-track components of Equation 10 can be fitted to the track and used to score its quality and predict upcoming

measurements, as per

$$\begin{bmatrix} \epsilon \\ \alpha \end{bmatrix}^{\mathcal{R}} \approx \frac{r_o}{a_o} \begin{bmatrix} x_1 - x_2(\cos(f_o - x_3) + \frac{e_o}{2} \cos(2f_o - x_3)) \\ x_4 + x_5 \sin(f_o + \omega - x_6) \end{bmatrix} \quad (12)$$

where  $x_{1,\dots,6}$  are scaled ROE equivalents in bearing angle space. Terms  $r, a, f, e, \omega$  can be computed from the absolute orbit estimate, and thus given at least three track measurements,  $x_{1,\dots,6}$  can be solved for via least squares. Kinematic rules are also derived from Equation 10 and Figure 2 to determine which hypotheses are physically reasonable. Briefly, 1) track velocities must be below a set maximum, 2) track velocities must be consistent over time, 3) tracks should generally not feature acute angles, 4) tracks should turn in a consistent direction, and 5) new data must be close to the predicted measurement.

Only tracks which pass all rules are propagated, and tracks are scored on how well they match expected kinematic behavior. Expected swarm maneuvers can be assigned to tracks by matching qualitative similarities between changes in  $x_{1,\dots,6}$  pre- and post-maneuver to expected changes in the ROE from a state transition matrix [34]. Mathematical detail is provided in [18]. The linearization of Equation 10 means that this procedure is most appropriate for inter-spacecraft separations up to several hundred kilometers, and not constellations at very large separations. However, on the shorter timescales between subsequent images that are small fractions of the orbit, the linearized model and associated kinematic rules can still enable target tracking prior to SOD initialization. In the future, more robust methods will be developed to fully treat the constellation case.

## 2. Batch Orbit Determination

The BOD module must produce orbit estimates for the system with sufficient accuracy to initialize the SOD module, using only a single coarse estimate of the observer orbit and batches of bearing angles to each target from the onboard VBS. Typical measurement collection periods are 1-2 orbits of the local observer. State estimation is accomplished using a new algorithm [19] that applies the following procedure for each target.

First, a 1-D family of state estimates is computed for specified samples of  $\delta\lambda$  using iterative batch least squares refinement, where the refined state consists of target ROE and the observer semimajor axis. Usage of this sampling approach is informed by a system observability analysis: in swarms and formation-flying scenarios, there is the underlying assumption of a weakly observable mode in mean along-track separation [16], whereas for more general configurations (e.g. constellations) this is not always the case. A typical choice is to divide the expected state space for  $\delta\lambda$  into 100-200 intervals in the positive and negative directions. The output state estimate is that which produces the least measurement residuals. A conceptual illustration for a single target is shown in Figure 5. It is important to minimize computation costs of sampling and thus, an analytic dynamics model is used when propagating the refined state to each measurement epoch. In LEO, the  $J_2$  oblateness perturbation is generally dominant. However, in lunar and cislunar scenarios,  $J_2, J_3$ , and third-body Earth and solar gravity can all be significant. Long-term effects due to these terms as described in Section II are therefore included in the lunar BOD module.

Next, the measurement noise matrix for each measurement (denoted  $\mathbf{R}_{\text{vbs}}$ ) is estimated using the measurement residuals corresponding to the final state estimate. Then, the covariance for estimated state components  $\mathbf{P}_{\text{est}}$  is computed via

$$\mathbf{P}_{\text{est}} = \mathbf{Y}_{\text{est}}^* (\mathbf{R}_{\text{vbs}} + \mathbf{Y}_{\text{prior}} \mathbf{P}_{\text{prior}} \mathbf{Y}_{\text{prior}}^T) \mathbf{Y}_{\text{est}}^{*T} \quad (13)$$

where  $\mathbf{Y}_{\text{est}}^*$  is the pseudoinverse of the measurement sensitivity matrix for estimated state components,  $\mathbf{Y}_{\text{prior}}$  is the measurement sensitivity matrix for a-priori information (e.g. orbit elements other than the semimajor axis), and  $\mathbf{P}_{\text{prior}}$  is the uncertainty of a-priori information. This formulation allows BOD to seamlessly transition between domains where uncertainty is driven by sensor performance or by errors in the a-priori information.

## 3. Sequential Orbit Determination

The SOD module continually refines orbit estimates and auxiliary state estimates of the observer and its targets by seamlessly fusing measurements from all observers transmitted over the ISL. SOD applies the bearing angle measurement model and numerical GVE dynamics model from Section II within a UKF framework. The choice of a UKF with an OE and ROE state parametrization provides crucial advantages. First, the weakly observable range to each target is primarily captured by  $\delta\lambda$  in most relative motion geometries, with other ROE being strongly observable [24]. This allows ARTMS to maximize accuracy by applying separate state estimation techniques to different components (as seen in BOD). Second, the UKF is able to incorporate nonlinearities in the dynamics and measurement models and preserves higher-order moments in the probability distribution, which enables angles-only observer and target state convergence without maneuvers. Third, OE and ROE states vary slowly with time, which allows accurate numerical integration of the GVE with large timesteps for efficient onboard orbit propagation.

Estimation of observer clock offsets and drift rates aids robustness and minimizes necessary ground contact. If clock offsets are not regularly updated, there exists growing mismatches between the epochs of ISL measurements and the local ARTMS instance,

leading to measurement errors and subsequent state biases and divergence. Within SOD, clock offsets are accounted for by propagating the local state estimate to the estimated epoch of the relevant measurement, determined by the observer’s onboard clock for local measurements or by the received time-tag plus the estimated differential clock offset for remote measurements. Inclusion of ballistic coefficients in the state reduces errors for high-altitude orbits (e.g. NRHO) in which SRP is a significant perturbation. If differential ballistic coefficients are not included, biases in the ROE state estimates are produced.

Three additional features maximize performance. First, adaptive process noise estimation is used to improve convergence speed and robustness to errors in the dynamics model [16]. Second, the state definition is organized to exploit the structure of the Cholesky factorization, reducing calls to the orbit propagator by almost a factor of two [35]. Third, measurements from remote observers are assigned to local targets for distributed stereo-vision. Care must be taken to prevent the ambiguities of assigning multiple measurements to the same target or assigning the same measurement to multiple targets. Selection criteria are developed based on Mahalanobis distance thresholds for a) matching orbit estimates broadcast by remote observers to local orbit estimates of targets, and b) matching estimated bearing angles of local targets to bearing angles broadcast by remote observers [20]. Unambiguous correspondence must be achieved such that only one choice lies within a Mahalanobis assignment region and no other choices lie within a Mahalanobis exclusion region. Figure 6 provides a conceptual example for b).

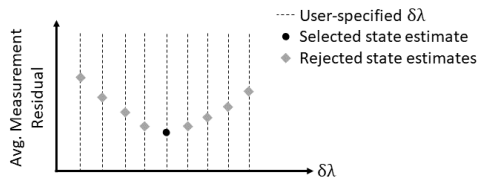


**Figure 5:** Conceptual illustration of converged measurement residuals for rejected (gray) and selected (black) state estimates for specified  $\delta\lambda$  values in BOD.

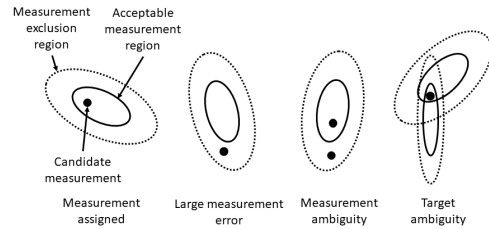


**Figure 6:** Illustration of conditions in which measurement assignment criteria are satisfied (left) and conditions that violate measurement assignment criteria (right).

#### IV. OBSERVABILITY ANALYSIS

Challenging observability conditions are encountered when estimating absolute and relative swarm or constellation orbits with angles-only measurements [19] [20] [36]. It is valuable to conduct an observability analysis for the lunar scenario to quantify potential state estimation performance and inform the design and tuning of algorithms employed in ARTMS. This paper applies the methodology of Koenig [19] [20] in which a lower bound for the state covariance matrix is computed from a measurement sensitivity matrix and measurement noise matrix.

##### 1. Numerical Observability Model

Consider a model providing inertial bearing angle measurements  $z$  as a function of system state  $x$ , local observer  $o$ , estimation epoch  $t_{est}$ , and measurement epoch  $t$ , of the form

$$z(t) = h(x, o, t_{est}, t) \quad (14)$$

Let bearing angles be provided at  $N$  epochs  $t_1, \dots, t_N$ , collectively referred to as  $\mathbf{t}_m$ . Additionally, let there be  $M$  swarm observers  $o_1, \dots, o_M$ , collectively referred to as  $\mathbf{o}_s$ . Define the clock error  $c_{err}(o, t)$  of observer  $o$  at epoch  $t$ . Then, the batch of measurements received by a single observer from all swarm observers at specific epoch  $t$  is

$$\mathbf{y}_o(t) = (h(x, o_1, t_{est}, t + c_{err}(o_1, t)), \dots, h(x, o_M, t_{est}, t + c_{err}(o_M, t)))^T \quad (15)$$

and across all epochs, the batch of measurements received by a single observer from all swarm observers is

$$\mathbf{y} = g(x, \mathbf{o}_s, t_{est}, \mathbf{t}_m) = (\mathbf{y}_o(t_1), \dots, \mathbf{y}_o(t_N))^T \quad (16)$$

Here, measurements are obtained by numerical integration of the GVE for all swarm or constellation members, as per Section II, from  $t_{est}$  to each measurement epoch. Measurements are computed from the propagated orbits. It is then necessary to evaluate the partial derivatives of measurements with respect to each component of  $x$ , for

$$\mathbf{Y}_{est}(x) = \left. \frac{\partial g(x, \mathbf{o}_s, t_{est}, \mathbf{t}_m)}{\partial x_{est}} \right|_x \quad (17)$$

where  $\mathbf{x}_{\text{est}}$  are the estimated components of  $\mathbf{x}$ . The partial derivatives for each specific measurement are computed numerically via central difference, using

$$\left. \frac{\partial \mathbf{h}}{\partial \mathbf{x}} \right|_{\mathbf{x}} = \frac{\mathbf{h}(\mathbf{x} + \Delta \mathbf{x}, o, t_{\text{est}}, t) - \mathbf{h}(\mathbf{x} - \Delta \mathbf{x}, o, t_{\text{est}}, t)}{2\|\Delta \mathbf{x}\|} \quad (18)$$

where  $\Delta \mathbf{x}$  is a vector that is zero except for the specific state component where sensitivity is being evaluated. Sizes used for the central difference are 10 m for semimajor axis,  $1/a_o$  for other orbit elements, 10 m for ROE, 0.1 seconds for clock drift, 1 ns/s for clock drift rates, and 0.001 for ballistic coefficients.

The observability analysis is based on the following model [19] for the relationship between the covariance matrix  $\mathbf{R}$  for the complete measurement batch, and the covariance matrix  $\mathbf{P}_{\text{est}}$  for the estimated state, given by

$$\mathbf{R} = \mathbf{Y}_{\text{est}}(\mathbf{x}) \mathbf{P}_{\text{est}} \mathbf{Y}_{\text{est}}^\top(\mathbf{x}) \quad (19)$$

When  $\mathbf{Y}_{\text{est}}$  is full column rank (true for all scenarios studied here),  $\mathbf{P}_{\text{est}}$  can be computed as

$$\mathbf{P}_{\text{est}} = (\mathbf{Y}_{\text{est}}^\top(\mathbf{x}) \mathbf{Y}_{\text{est}}(\mathbf{x})) (\mathbf{Y}_{\text{est}}^\top(\mathbf{x}) \mathbf{R} \mathbf{Y}_{\text{est}}(\mathbf{x})) (\mathbf{Y}_{\text{est}}^\top(\mathbf{x}) \mathbf{Y}_{\text{est}}(\mathbf{x}))^{-1} \quad (20)$$

The matrix  $\mathbf{R}$  assumes independent measurements with identical noise distributions, no uncertainty in a-priori state information, and perfect knowledge of dynamics [19].  $\mathbf{P}_{\text{est}}$  thus provides an indication of a lower bound for achievable estimation accuracy for the given number of measurements. If  $\mathbf{R}_1$  is the measurement noise matrix for a single measurement,  $\mathbf{R}$  is

$$\mathbf{R} = \begin{bmatrix} \mathbf{R}_1 & \mathbf{0} & \dots & \mathbf{0} \\ \mathbf{0} & \mathbf{R}_1 & \dots & \mathbf{0} \\ \vdots & \vdots & \ddots & \vdots \\ \mathbf{0} & \mathbf{0} & \dots & \mathbf{R}_1 \end{bmatrix} \quad (21)$$

Observability of the complete system state is evaluated for five configurations, detailed in Tables 1 and 2. These configurations vary the number of observers, semimajor axis, eccentricity, target range, and the magnitude of relative motion, echoing the simulation scenarios explored in Section V. Formation types are E/I-vector separated or passive safety ellipse (PSE), in-train (IT) and constellation (CON). In-train formations are primarily separated in the along-track direction with  $\delta e \approx \delta i \approx 0$  and very little relative motion. PSE formations present more significant relative motion but retain similar absolute orbits for all spacecraft. Constellations feature large orbit element differences between spacecraft.

**Table 1:** Chief spacecraft initial state for observability analysis.

Scenario	Type	Swarm members	Swarm observers	$a$ (km)	$e$	$i$ ( $^\circ$ )	$\Omega$ ( $^\circ$ )	$\omega$ ( $^\circ$ )	$M_0$ ( $^\circ$ )	$c_{\text{err}}$ (s)	$d_{\text{err}}(\frac{ns}{s})$	$B$
A	LLO	4	2	1849.9	0.0497	89.0	166.0	270.0	0.0	1.0	1.0	0.02
B	LLO	4	2	1849.9	0.0497	89.0	166.0	270.0	0.0	1.0	1.0	0.02
C	ELFO	4	4	5053.7	0.6067	63.4	0.0	270.0	0.0	1.0	1.0	0.02
D	ELFO	4	4	5053.7	0.6067	63.4	0.0	270.0	0.0	1.0	1.0	0.02
E	NRHO	4	4	51350	0.9298	67.4	164.1	101.7	0.0	1.0	1.0	0.02

**Table 2:** Deputy spacecraft initial states for observability analysis.

Scenario	Type	$a\delta a$	$a\delta \lambda$ (km)	$a\delta e_x$	$a\delta e_y$ (km)	$a\delta i_x$	$a\delta i_y$ (km)	$\delta c_{\text{err}}$ (s)	$\delta d_{\text{err}}(\frac{ns}{s})$	$\delta B$
A	PSE	0	50, 100, 150	0	1.5, 3.0, 4.5	0	1.5, 3.0, 4.5	0.1	1.0	0.005
B	IT	0	50, 100, 150	0	0.15, 0.30, 0.45	0	0.15, 0.30, 0.45	0.1	1.0	0.005
C	PSE	0	50, 100, 150	-0.5, 0.5, 0	0.5, 0.5, -0.5	0	0.5, -0.5, -0.5	0.1	1.0	0.005
D	CON	0	-13240, 5400, -12850	0	0	0	-3870, -7730, 5560	0.1	1.0	0.005
E	PSE	0	50, 100, 150	-0.5, 0.5, 0	0.5, 0.5, -0.5	0	0.5, -0.5, -0.5	0.1	1.0	0.005

Bearing angles are subject to 20 arcsec of  $1\sigma$  noise, representative of errors from modern nanosatellite star trackers [37]. Two orbits of measurements are provided with 50 measurements per orbit at evenly-spaced intervals. Included perturbations during orbit propagation for measurement generation are a 5x5 lunar gravity model [38], a cannonball SRP model with cylindrical lunar shadow, and third-body Earth and Sun gravity. The dynamics numerical integration timestep is 60s. The spacecraft are modeled as 12U CubeSats with deployable solar panels, with a constant mass of 12kg and constant sun-facing cross-sectional area of 0.12 m<sup>2</sup>.

## 2. Numerical Results

Tables 3 and 4 present results from the observability analysis, where ‘-’ indicates that the state component was not estimated. The bar over each state component indicates an average value across all observers and targets. The analysis indicates that absolute and relative orbits are observable using angles-only measurements, as are clock offsets and ballistic coefficients when required. Absolute and relative orbits can potentially be estimated with position uncertainty on the order of hundreds of meters. Clock offsets can potentially be estimated to within one second. Recall that this analysis ignores the effects of uncertainty in the dynamics model and it is therefore expected that higher-fidelity simulations will display degraded performance for the same number of measurements, especially for highly-perturbed scenarios (e.g. at low altitudes for spherical harmonic gravity) or scenarios with long orbit periods and propagation times (e.g. at high altitudes in NRHO orbits).

Trends of the observability analysis correspond to expectations. Specifically, Scenario A displays improved uncertainty in absolute and relative position estimates compared to Scenario B, due to more observable relative motion displayed by the PSE formation. Increasing orbit eccentricity as in Scenario C improves absolute and relative position uncertainty because additional relative motion is introduced by the eccentricity. Scenario D displays improved absolute position uncertainty due to the more distinct absolute orbits and measurement baselines of the constellation; however, relative position uncertainty is worsened by the much larger target ranges. Scenario E displays large tangential position uncertainties due to comparatively slow orbit dynamics and measurement variations at high altitudes. Higher altitudes make the clock offset more challenging to estimate, while clock drift rate uncertainty is improved by higher eccentricities.

**Table 3:** Absolute state component uncertainty from quantitative observability analysis.

Scenario	$\overline{\sigma_{r_R}}$ (m)	$\overline{\sigma_{r_T}}$ (m)	$\overline{\sigma_{r_N}}$ (m)	$\overline{\sigma_{v_R}}$ (mm/s)	$\overline{\sigma_{v_T}}$ (mm/s)	$\overline{\sigma_{v_N}}$ (mm/s)	$\overline{\sigma_{c_{\text{err}}}}$ (s)	$\overline{\sigma_{d_{\text{err}}}}$ ( $\frac{\mu\text{s}}{\text{s}}$ )	$\overline{\sigma_B}$
A	91	300	180	94	160	360	-	-	-
B	110	650	110	94	190	360	-	-	-
C	140	240	120	21	32	14	-	-	-
D	46	94	82	5.4	9.3	6.9	-	-	-
E	290	860	520	3.2	3.4	3.5	-	-	-

**Table 4:** Relative state component uncertainty from quantitative observability analysis.

Scenario	$\overline{\sigma_{\delta r_R}}$ (m)	$\overline{\sigma_{\delta r_T}}$ (m)	$\overline{\sigma_{\delta r_N}}$ (m)	$\overline{\sigma_{\delta v_R}}$ (mm/s)	$\overline{\sigma_{\delta v_T}}$ (mm/s)	$\overline{\sigma_{\delta v_N}}$ (mm/s)	$\overline{\sigma_{\delta c_{\text{err}}}}$ (ms)	$\overline{\sigma_{\delta d_{\text{err}}}}$ ( $\frac{\mu\text{s}}{\text{s}}$ )	$\overline{\sigma_{\delta B}}$
A	15	270	14	5.6	14	4.9	46	2.4	-
B	37	740	13	6.0	35	3.0	55	3.2	-
C	61	92	2.7	8.9	5.5	0.24	190	2.0	$1.3 \times 10^{-3}$
D	150	140	160	23	24	27	130	1.6	$4.1 \times 10^{-2}$
E	200	140	0.60	2.2	0.54	0.031	1600	1.7	$4.7 \times 10^{-6}$

## V. SIMULATION

### 1. Simulation Scenarios

Five simulation scenarios are developed to validate the observability analysis and demonstrate the feasibility of autonomous angles-only navigation in lunar orbit for multi-agent space systems. Each scenario explores a different form of distributed lunar mission and consists of four spacecraft. Initial conditions are given in Tables 1 and 2. Absolute orbits are specified for a ‘chief’ observer and relative orbits are specified with respect to this observer.

Scenarios A and B present swarms in quasi-frozen low lunar orbits (LLO). Quasi-frozen orbits are specifically designed to ensure the mean orbit eccentricity vector remains nearly constant over time [39]. Applications include lunar monitoring, networking and distributed aperture science. Scenario A considers a PSE formation with significant relative motion. Scenario B considers an in-train formation with little relative motion.

Scenarios C and D present swarms in an elliptic lunar frozen orbit (ELFO). Scenario C is a PSE formation and Scenario D is a flower constellation. Flower constellations consist of repeating ground tracks with phased satellites that follow the same trajectory relative to the rotating frame of the central body [40]. Applications include lunar communications, observation, and global positioning systems.

Scenario E is a PSE formation in a 9:2 synodic L2 south near-rectilinear halo orbit (NRHO). The NRHO is highly elliptical, and NASA’s Lunar Orbital Platform-Gateway (LOP-G) is expected to apply a similar orbit. Applications for a swarm therefore include autonomous monitoring and remote sensing in support of LOP-G operations.

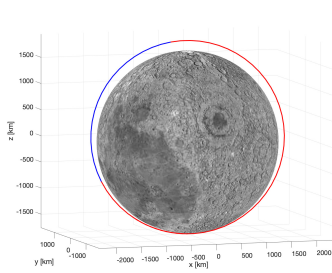
Each scenario presents very different measurement conditions. The LLO orbit is eclipsed for 30% of the orbit period, leading to large measurement gaps. In addition, orbit periods range between 2 hours (LLO), 9 hours (ELFO) and 150 hours (NRHO). The

frequency of camera measurements is scaled to provide  $\sim 60$  measurements per orbit, up to a maximum of 30 minutes between measurements. The SOD dynamics integration step size is scaled to provide  $\sim 200$  steps per orbit, up to a maximum of 300 seconds per step. Absolute orbits are plotted in Figure 7 and relative orbits are plotted in Figure 8.

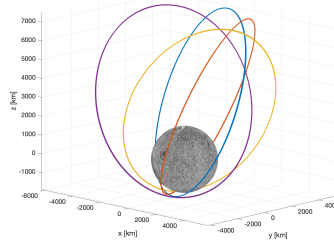
In Scenarios A and B, the leading and trailing spacecraft with respect to  $u$  act as observers. In Scenarios C-E, all spacecraft are observers. In Scenarios A-C, observer VBS are aligned with the (anti-)velocity direction depending on where most targets are visible. In Scenarios D and E, relative motion is large and not all targets remain within the FOV. In response, observers perform active tracking and point at each target in a cyclic fashion in successive measurement epochs. An autonomous BOD initialization is used for Scenarios A-C while an external ground initialization is used for Scenarios D and E. Conditions are summarized in Table 5.

**Table 5:** Summary of simulation conditions.

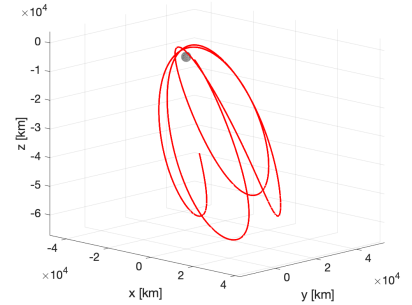
Scenario	Abs. Orbit	Rel. Orbit	Period	Sim. Length	Eclipses	Observers	Attitude	IMP Meas. Frequency	SOD Dyn. Step Size	Initialization Method
A	LLO	PSE	2 hrs	24 hrs	30%	2	Passive	120 s	30 s	BOD
B	LLO	IT	2 hrs	24 hrs	30%	2	Passive	120 s	30 s	BOD
C	ELFO	PSE	9 hrs	48 hrs	0%	4	Passive	480 s	120 s	BOD
D	ELFO	CON	9 hrs	48 hrs	0%	4	Active	480 s	120 s	Ground
E	NRHO	PSE	150 hrs	600 hrs	0%	4	Active	1800 s	300 s	Ground



(a) Quasi-frozen LLO (Scenario A)



(b) ELFO flower constellation (Scenario D)



(c) NRHO (Scenario E)

**Figure 7:** Absolute orbit of the chief satellite for each simulation case in the MCI frame. For the quasi-frozen LLO, eclipses are in blue and non-eclipse regions are in red. For the flower constellation, each color corresponds to a different satellite.

## 2. Data Generation

Ground truth positions and velocities of the four-spacecraft system are obtained by numerically integrating the GVE. Included perturbations are summarized in Table 6. As before, spacecraft are modeled as 12U CubeSats with a constant mass of 12kg and constant sun-facing cross-sectional area of  $0.12 \text{ m}^2$ . Target visibility and visual magnitudes are computed using a model which takes into account the observer-target-Sun phase angle and variations in reflected flux from different satellite surfaces [41]. Ground truth clocks and clock noise are propagated using the Galleani model which includes both frequency and phase noise [42]. Clock quality emulates the Microsemi SA.45s chip-scale atomic clock with an Allan deviation of  $10^{-10}$  for  $\tau = 1$  second [43]. Noise values of  $q_1 = (3 \times 10^{-10})^2$  and  $q_2 = (3 \times 10^{-14})^2$  are applied in the clock model.

Measurements are then synthesized from the ground truth. VBS images are generated using 3D vector graphics in OpenGL [44]. Visual magnitudes, angles, and proper motions of stars are obtained from the Hipparcos star catalog and objects within the camera FOV are rendered using Gaussian point spread functions. Mismatches between known and true camera parameters induce additional ( $5''$ ,  $5''$ ) bearing angle errors ( $1\sigma$ ). Spacecraft possess ( $6''$ ,  $6''$ ,  $30''$ ) of x-y-z attitude control error ( $1\sigma$ ). LLO simulations also include a CubeSat star tracker in the loop. Input images are retrieved from a Blue Canyon Technologies Nano Star Tracker as simulated by the Stanford SLAB Optical Simulator (OS). The OS is a variable-magnification testbed consisting of two lenses and a microdisplay. Synthetic space scenes are generated and shown on the display and by moving the lenses and display relative to each other, the VBS under test is stimulated with appropriate magnification. The OS is calibrated such that the VBS image is similar in radiosity and geometry to what would be observed in orbit. Development, calibration, and usage of the OS are detailed in [44] with achievable errors between desired and measured bearing angles of less than  $10''$ .

Inputs are processed by ARTMS in the form of multi-satellite simulation in MATLAB Simulink and C++. The SOD dynamics integration timestep and IMP measurement frequencies are provided in Table 5 for each scenario. Perturbations modeled within

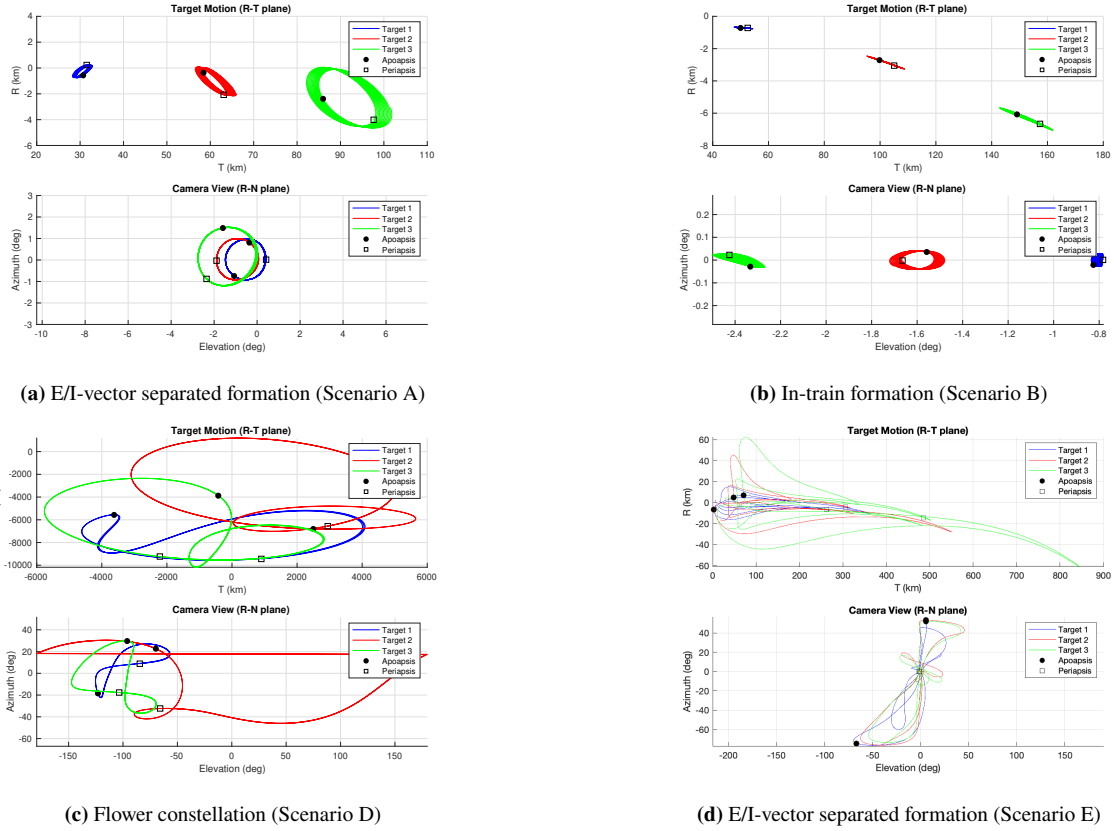


**Figure 8:** Relative positions of targets with respect to the primary observer in the RT plane (top) and RN plane (bottom). The black circle shows relative positions at apolune and the white square shows relative positions at perilune.

SOD and errors in the coarse observer absolute state initialization (from the DSN) and relative state initialization (Scenarios D/E only) are summarized in Table 6. Autonomous BOD initialization occurs after 4 hours when applied. Covariance matching is applied in SOD for adaptive process noise and empirical accelerations are not estimated.

**Table 6:** Summary of dynamics models and state initialization errors.

Model	Lunar gravity model (GRGM1200A [38])	Third body gravity	Solar radiation pressure	State Initialization Error ( $1\sigma$ )				
				RTN position	RTN velocity	$B$	Clock drift	Clock drift rate
Ground truth	60x60	Earth, Sun	Cannonball	-	-	-	-	-
SOD	10x10	Earth, Sun	Cannonball	(100, 1000, 100) m	(0.1, 1, 0.1) m/s	0.004	1 s	1 $\mu$ s/s
BOD	3x3	Earth, Sun	-	(100, 1000, 100) m	(0.1, 1, 0.1) m/s	-	-	-

### 3. Simulation Results

Mean estimation errors for all simulation scenarios are summarized in Table 7-8, where steady-state values are computed as averages across the final orbit. As expected, state estimation errors produced by the simulations are of a similar order but somewhat larger than those in Tables 3-4, because the observability analysis assumed perfect knowledge of dynamics and a-priori state information. Performance differences are most significant in the highly elliptic orbits of Scenarios C-E, in which the filter dynamics model is used to propagate states for longer time periods. However, the trends displayed when comparing different scenarios are similar, which aids in validating the analysis methods. For example, Scenario B presents worse performance than Scenario A for both methods, and Scenario C presents better relative orbit results but worse absolute orbit results than Scenario D for both methods. The reasoning behind these trends and others is discussed below.

**Table 7:** Mean state error and  $1\sigma$  state uncertainty at steady state for the observer absolute state estimate.

Scenario	$\delta r_R$ (m)	$\delta r_T$ (m)	$\delta r_N$ (m)	$\delta v_R$ (mm/s)	$\delta v_T$ (mm/s)	$\delta v_N$ (mm/s)
A	$9 \pm 150$	$355 \pm 326$	$-2 \pm 142$	$29 \pm 132$	$-55 \pm 262$	$12 \pm 120$
B	$-66 \pm 205$	$98 \pm 496$	$-1 \pm 186$	$14 \pm 181$	$60 \pm 360$	$29 \pm 157$
C	$253 \pm 2513$	$538 \pm 3507$	$-711 \pm 1549$	$46 \pm 487$	$20 \pm 564$	$-20 \pm 165$
D	$-151 \pm 493$	$40 \pm 535$	$50 \pm 383$	$1 \pm 137$	$14 \pm 156$	$-24 \pm 128$
E	$-4353 \pm 6170$	$749 \pm 2606$	$2777 \pm 3089$	$-36 \pm 50$	$13 \pm 31$	$2 \pm 16$

**Table 8:** Mean state error and  $1\sigma$  state uncertainty at steady state for target relative state estimates.

Scenario	Target	$\delta r_R$ (m)	$\delta r_T$ (m)	$\delta r_N$ (m)	$\delta v_R$ (mm/s)	$\delta v_T$ (mm/s)	$\delta v_N$ (mm/s)	Clock Drift (ms)	Clock Drift Rate ( $\mu\text{s/s}$ )
A	1	$27 \pm 18$	$-274 \pm 136$	$1 \pm 7$	$0 \pm 14$	$-16 \pm 21$	$1 \pm 6$	$-3 \pm 10$	$-0.28 \pm 0.41$
	2	$17 \pm 12$	$-196 \pm 97$	$0 \pm 4$	$0 \pm 9$	$-13 \pm 14$	$1 \pm 4$		
	3	$7 \pm 6$	$-95 \pm 55$	$-1 \pm 2$	$0 \pm 5$	$-8 \pm 7$	$0 \pm 2$		
B	1	$4 \pm 15$	$-47 \pm 134$	$-2 \pm 5$	$3 \pm 11$	$-4 \pm 17$	$0 \pm 5$		
	2	$13 \pm 32$	$-111 \pm 234$	$-3 \pm 10$	$5 \pm 21$	$-8 \pm 33$	$1 \pm 9$		
	3	$18 \pm 49$	$-126 \pm 312$	$-4 \pm 15$	$7 \pm 31$	$-9 \pm 47$	$1 \pm 13$	$-6 \pm 22$	$-1.57 \pm 2.79$
C	1	$-6 \pm 41$	$9 \pm 67$	$1 \pm 10$	$-1 \pm 12$	$1 \pm 12$	$0 \pm 2$	$14 \pm 21$	$0.15 \pm 0.24$
	2	$-11 \pm 79$	$22 \pm 132$	$2 \pm 19$	$-3 \pm 23$	$1 \pm 22$	$0 \pm 4$	$1 \pm 20$	$0.13 \pm 0.23$
	3	$-20 \pm 122$	$33 \pm 199$	$3 \pm 29$	$-2 \pm 36$	$3 \pm 32$	$0 \pm 5$	$8 \pm 21$	$0.26 \pm 0.25$
D	1	$-121 \pm 1620$	$-316 \pm 1617$	$-129 \pm 944$	$-89 \pm 563$	$-85 \pm 440$	$31 \pm 213$	$233 \pm 780$	$-6.23 \pm 16.53$
	2	$-288 \pm 1536$	$-267 \pm 1656$	$63 \pm 1335$	$-24 \pm 401$	$10 \pm 467$	$19 \pm 275$	$164 \pm 1988$	$0.26 \pm 34.17$
	3	$-35 \pm 1925$	$-222 \pm 1736$	$-275 \pm 1439$	$-16 \pm 630$	$-5 \pm 454$	$27 \pm 330$	$380 \pm 1168$	$10.81 \pm 24.00$
E	1	$-19 \pm 35$	$-10 \pm 43$	$15 \pm 15$	$0 \pm 1$	$0 \pm 1$	$0 \pm 0$	$-719 \pm 161$	$-0.47 \pm 0.28$
	2	$-89 \pm 96$	$-104 \pm 80$	$178 \pm 119$	$0 \pm 2$	$1 \pm 2$	$1 \pm 1$	$93 \pm 143$	$0.08 \pm 0.27$
	3	$-54 \pm 123$	$-31 \pm 106$	$106 \pm 162$	$0 \pm 2$	$2 \pm 3$	$0 \pm 1$	$1020 \pm 139$	$0.20 \pm 0.26$

a). Scenario A (PSE Formation in LLO)

Figure 9 presents relative navigation results for Scenario A, where time  $t = 0$  in the plot corresponds to the initialization of SOD. The majority of position error occurs in the along-track direction as it is analogous to the weakly observable target range. Other components of target motion are more observable and see the correspondingly smaller error. Differential clock offsets and drift rates are effectively estimated - despite large initial errors, offsets are estimated to within 0.01 s and drift rates to within  $0.5 \mu\text{s/s}$ . Convergence to steady state is achieved after approximately 5 orbits even in the presence of eclipse periods, indicating good performance under challenging measurement conditions. State uncertainties observe periodic behavior due to eclipse periods during which measurements are unavailable.

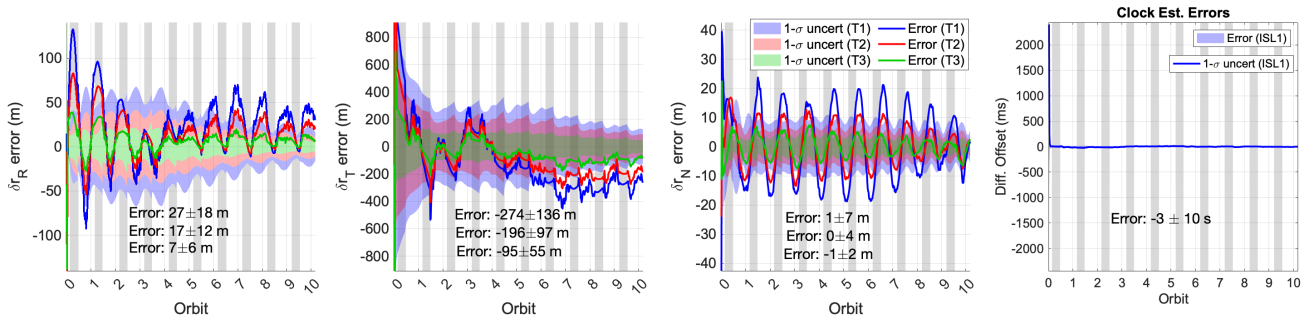


**Figure 9:** Relative orbit estimation errors for the chief observer in Scenario A. Statistics are computed over the last orbit.

b). Scenario B (In-train Formation in LLO)

Performance is degraded in the in-train formation compared to the PSE formation. In-train formations are comparatively more challenging to track because relative motion is small and  $\delta\lambda$  is only weakly observable. Nevertheless, it is still possible to achieve orbit determination and clock synchronization using angles-only measurements. Multiple observers provide improved performance via stereo measurements and orbit eccentricity introduces additional relative motion between in-train targets.

c). Scenario C (PSE Formation in ELFO)

Orbit estimates for the ELFO swarm are significantly more uncertain than in LLO. Reasons for these trends can be found in Figure 10, which shows mean estimation errors, mean relative acceleration, mean relative velocity, and mean target range throughout the final orbit and at apolune and perilune specifically. There is a clear correlation between absolute orbit estimation error and the relative acceleration of the satellites within the swarm or constellation: as the relative acceleration becomes larger, absolute orbit estimation is improved. This is because ARTMS can exploit larger differences in relative perturbations and nonlinear dynamics to resolve absolute orbit ambiguity. Thus, at higher altitudes with weaker gravity (produced by more elliptic orbits), absolute orbit estimates are degraded compared to the LLO case. Furthermore, larger relative velocity leads to larger relative orbit estimation errors. When relative motion is faster, the propagated error arising from dynamics modeling uncertainty will be larger between measurement updates. Larger gravitational accelerations near perilune also increase the deviation of filter dynamics from the true dynamics, which reduces filter performance. Note that in the LLO scenarios, relative state estimation errors are larger at the apolune, which appears to be a contradiction at first glance. However, this is due to the eclipse periods before the apolune passage (c.f. Figure 7) during which measurements are unavailable and the covariance increases.

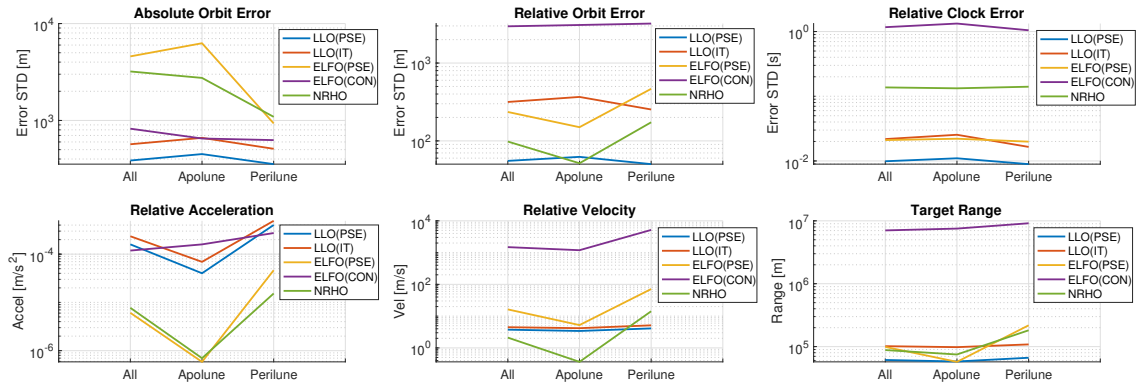


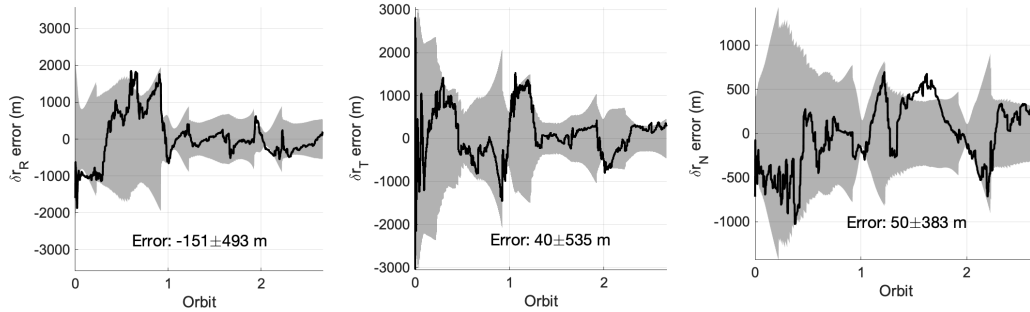
**Figure 10:** The mean standard deviation of the absolute position estimate (upper left), relative position estimate (upper middle), and relative clock estimate (upper right), with the mean magnitude of relative acceleration (lower left), relative velocity (lower middle), and target range (lower right).

d). Scenario D (ELFO Flower Constellation)

Absolute state estimation results for the flower constellation are shown in Figure 12. Compared to Scenario C, absolute orbit estimates are much improved. This is because the satellite orbits are much more distinct, with subsequently larger differences in orbit perturbations that ARTMS is able to exploit and more distinct measurement baselines. However, relative orbit estimates are worsened in the constellation. Figure 10 shows the relationship between relative state estimation accuracy and target range, where estimation accuracy decreases as the target range increases. This is because as the target range becomes larger, the VBS measurement error corresponds to larger uncertainties in the ROE state. Differential clock offsets are coupled with the ROE state via the bearing angle measurement model (c.f. Eq.(15)) and are estimated by comparing differences in target bearing angles as measured by distinct observers, and this effect therefore increases the uncertainty of differential clock estimates also. Overall, the good absolute orbit determination accuracy achieved in the constellation case indicates the potential of leveraging ARTMS to provide lunar PNT services. However, new challenges also arise from the larger variation in target relative positions. For typical FOV, targets can no longer be consistently measured by passive camera tracking and more complex active target tracking becomes necessary to achieve regular swarm measurements. This paper assumes that after initialization, VBS are pointed at each target in sequence to obtain regular measurement updates. However, this is not necessarily optimal and does not treat the issue of pre-initialization target tracking for which target state information is unavailable. The development of new, efficient task distribution and attitude optimization algorithms for target tracking will therefore play a key role.

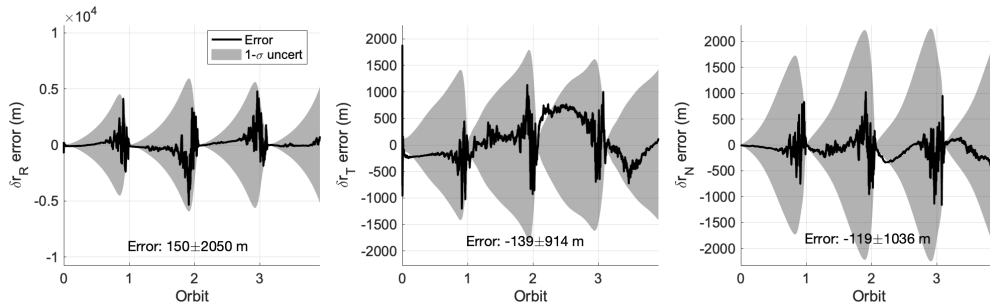
e). Scenario E (PSE Formation in NRHO)

Figure 12 presents absolute state estimation results for Scenario E. The NRHO estimation results are characterized by periodic growth and shrinkage of state estimate covariance. Particular challenges are faced near apolune, where uncertainties increase to several kilometers. This is due to the extremely slow system dynamics and smaller relative accelerations. Measurements are thus very similar for successive IMP samples and the information provided by measurement updates is limited. Time synchronization similarly proves challenging and clock errors venture outside the  $1\sigma$  covariance bounds. The ground truth clock model includes random process noise [42], the ARTMS clock initialization includes errors, and the long state propagation times produce greater



**Figure 11:** Absolute orbit estimation errors for the chief observer in Scenario D. Statistics are computed over the last orbit.

inaccuracies during SOD clock propagation. Furthermore, the limited effectiveness of measurement updates makes it difficult to maintain robust clock estimate convergence. Modifications may be required to improve NRHO clock estimates such as sharing of clock estimates over the ISL (in addition to orbit estimates and bearing angles) in a more distributed fashion. Degradation of relative state estimation is minimized by comparison due to the fully connected measurement network of four swarm observers.



**Figure 12:** Absolute orbit estimation errors for the chief observer in Scenario E. Statistics are computed over the last orbit.

## VI. CONCLUSION

This research presents an architecture for autonomous, distributed navigation and timekeeping for multi-agent space systems in lunar orbit, using angles-only measurements obtained by onboard cameras. The proposed Angles-only Absolute and Trajectory Measurement System (ARTMS) consists of three novel algorithms: Image Processing, which identifies targets in images using multi-hypothesis tracking and computes their bearing angles; Batch Orbit Determination, which computes a system state initialization from bearing angles batches using range sampling techniques; and Sequential Orbit Determination, which uses an unscented Kalman filter to refine the system state, seamlessly fusing measurements from multiple observers.

Theoretical performance bounds from a numerical observability analysis and computation of the estimated state covariance show that depending on the absolute orbit and system geometry, absolute orbits are observable with an accuracy on the order of hundreds of meters to several kilometers, while relative orbits can potentially be estimated with errors of several hundred meters in  $\delta\lambda$  and tens of meters for other relative orbit elements (ROE). Clock offsets are observable to within one second with angles-only measurements. The observability analysis is validated by high-fidelity camera-in-the-loop simulations of five different scenarios in a low lunar orbit (LLO), elliptic frozen orbit (ELFO), and near-rectilinear halo orbit (NRHO). For the LLO scenarios, both absolute and relative state estimates successfully converge even in the presence of eclipse periods and in a less observable in-train configuration. For the ELFO scenario, an absolute orbit estimation error of 250 m is achieved in a flower constellation, more than 10 times smaller than errors for a comparable passive safety ellipse formation. Constellations are a promising application for ARTMS because satellite orbits are very distinct, resulting in improved system observability, but new active target tracking algorithms are likely required to achieve regular target measurements. In the NRHO scenario, the high eccentricity leads to highly variable dynamical speeds and periodic covariance growth and reduction. However, by increasing the number of measurement cross-links within the swarm, relative positions are estimated with 100 m accuracy and absolute orbit convergence is maintained. Overall, simulations display promising navigation performance for a variety of system geometries and orbits in the lunar region.

Future research areas include optimization of observer attitudes to ensure that targets remain in view for consistent observation at large separations and when in very distinct orbits. Including inter-satellite range measurements in addition to the angle measurements will also be explored, which is expected to improve both orbit and clock offset estimation accuracy by compensating for the weakly observable target range in angles-only navigation.

## ACKNOWLEDGEMENTS

The authors wish to acknowledge the contributions of Joshua Sullivan and Adam W. Koenig to the development of the ARTMS architecture. This research was partially funded by AFOSR award number: FA9550-21-1-0414.

## REFERENCES

- [1] K. C. Laurini and W. H. Gerstenmaier, "The global exploration roadmap and its significance for NASA," *Space Policy*, vol. 30, no. 3, pp. 149–155, 2014.
- [2] D. J. Israel, K. D. Mauldin, C. J. Roberts, J. W. Mitchell, A. A. Pulkkinen, D. C. La Vida, M. A. Johnson, S. D. Christe, and C. J. Gramling, "LunaNet: A flexible and extensible lunar exploration communications and navigation infrastructure," in *2020 IEEE Aerospace Conference*. IEEE, 2020, pp. 1–14.
- [3] T. Cozzens, "Galileo will help lunar pathfinder navigate around Moon," *GPS World*, 2021. [Online]. Available: [https://www.gpsworld.com/galileo-will-help-lunar-pathfinder-navigate-around-moon/?utm\\_source=Navigate!+Weekly+GNSS+News&utm\\_medium=Newsletter&utm\\_campaign=NCMCD210331002&oly\\_enc\\_id=6244C4859912F3Z](https://www.gpsworld.com/galileo-will-help-lunar-pathfinder-navigate-around-moon/?utm_source=Navigate!+Weekly+GNSS+News&utm_medium=Newsletter&utm_campaign=NCMCD210331002&oly_enc_id=6244C4859912F3Z)
- [4] H. Sanchez, D. McIntosh, H. Cannon, C. Pires, M. Field, J. Sullivan, S. D'Amico, L. Mall, and B. O'Connor, "Starling-1: Swarm Technology Demonstration," in *32nd Annual Small Satellite Conference*, Logan, UT, Aug. 2018.
- [5] M. D. Johnston, D. Tran, B. Arroyo, S. Sorensen, P. Tay, B. Carruth, A. Coffman, and M. Wallace, "Automated Scheduling for NASA's Deep Space Network," *AI Magazine*, vol. 35, no. 4, pp. 7–25, 2014.
- [6] G. E. Lanyi, J. S. Border, and D. K. Shin, "Radiometric spacecraft tracking for deep space navigation," in *Proceedings of the 2008 National Technical Meeting of The Institute of Navigation*, 2008, pp. 86–90.
- [7] V. Capuano, F. Basile, C. Botteron, and P.-A. Farine, "GNSS-based orbital filter for Earth Moon Transfer Orbits," *The Journal of Navigation*, vol. 69, no. 4, pp. 745–764, 2016.
- [8] M. Murata, I. Kawano, and K. Inoue, "Simulation Evaluation of Moon Transfer Orbit Navigation Using GPS Carrier Phases," *Proceedings of the 34th International Technical Meeting of the Satellite Division of The Institute of Navigation (ION GNSS+ 2021)*, pp. 1033–1038, 2021.
- [9] S. Bhamidipati, T. Mina, and G. Gao, "Design Considerations of a Lunar Navigation Satellite System with Time-Transfer from Earth-GPS," *Proceedings of the 34th International Technical Meeting of the Satellite Division of The Institute of Navigation (ION GNSS+ 2021)*, pp. 950–965, 2021.
- [10] K.-M. Cheung, C. Lee, and D. Heckman, "Feasibility of 'weak GPS' real-time positioning and timing at lunar distance," in *2020 IEEE Aerospace Conference*. IEEE, 2020, pp. 1–7.
- [11] K. Iiyama, Y. Kawabata, and R. Funase, "Autonomous and Decentralized Orbit Determination and Clock Offset Estimation of Lunar Navigation Satellites Using GPS Signals and Inter-Satellite Ranging," *Proceedings of the 34th International Technical Meeting of the Satellite Division of The Institute of Navigation (ION GNSS+ 2021)*, pp. 936–949, 2021.
- [12] "ESA, NASA race to the Moon for first lunar GNSS fix," *Inside GNSS*, Mar 2021. [Online]. Available: <https://insidegnss.com/esa-nasa-race-to-the-moon-for-first-lunar-gnss-fix/>
- [13] "Galileo will help Lunar Pathfinder navigate around Moon," Mar 2021. [Online]. Available: [https://www.esa.int/Applications/Navigation/Galileo\\_will\\_help\\_Lunar\\_Pathfinder\\_navigate\\_around\\_Moon](https://www.esa.int/Applications/Navigation/Galileo_will_help_Lunar_Pathfinder_navigate_around_Moon)
- [14] S. D'Amico, J.-S. Ardaens, G. Gaias, H. Benninghoff, B. Schlepp, and J. L. Jørgensen, "Noncooperative Rendezvous Using Angles-Only Optical Navigation: System Design and Flight Results," *Journal of Guidance, Control, and Dynamics*, vol. 36, no. 6, pp. 1576–1595, Nov. 2013.
- [15] J.-S. Ardaens and G. Gaias, "Angles-only relative orbit determination in low earth orbit," *Advances in Space Research*, vol. 61, no. 11, pp. 2740–2760, 2018.
- [16] J. Sullivan, A. W. Koenig, J. Kruger, and S. D'Amico, "Generalized Angles-Only Navigation Architecture for Autonomous Distributed Space Systems," *Journal of Guidance, Control, and Dynamics*, vol. 44, no. 6, pp. 1087–1105, 2021.

- [17] A. W. Koenig, J. Kruger, and S. D'Amico, "ARTMS: Enabling Autonomous Distributed Angles-Only Orbit Estimation for Spacecraft Swarms," in *American Control Conference*, New Orleans, Louisiana, 2021.
- [18] J. Kruger and S. D'Amico, "Autonomous angles-only multitarget tracking for spacecraft swarms," *Acta Astronautica*, vol. 189, pp. 514–529, 2021.
- [19] A. W. Koenig and S. D'Amico, "Observability-Aware Numerical Algorithm for Angles-Only Initial Relative Orbit Determination," in *2020 AAS/AIAA Astrodynamics Specialist Conference*, Lake Tahoe, California, 2020.
- [20] J. Kruger, A. W. Koenig, and K. Wallace, "Autonomous Angles-Only Navigation for Spacecraft Swarms around Planetary Bodies," in *IEEE Aerospace Conference Proceedings*, Big Sky, Montana, Mar. 2021.
- [21] D. A. Vallado and W. D. McClain, *Fundamentals of Astrodynamics and Applications*, 4th ed. Hawthorne, California: Microcosm Press, 2013.
- [22] S. D'Amico, "Autonomous Formation Flying in Low Earth Orbit." PhD Thesis, Delft University, 2010, oCLC: 839641932.
- [23] A. W. Koenig, T. Guffanti, and S. D'Amico, "New State Transition Matrices for Relative Motion of Spacecraft Formations in Perturbed Orbits," *Journal of Guidance, Control, and Dynamics*, Sep. 2016.
- [24] J. Sullivan and S. D'Amico, "Nonlinear Kalman Filtering for Improved Angles-Only Navigation Using Relative Orbital Elements," *Journal of Guidance, Control, and Dynamics*, pp. 1–18, Jul. 2017.
- [25] K. T. Alfriend, Ed., *Spacecraft Formation Flying: Dynamics, Control, and Navigation*, ser. Elsevier astrodynamics series. Oxford: Butterworth-Heinemann/Elsevier, 2010, oCLC: 699265912.
- [26] D. Brouwer, "Solution of the problem of artificial satellite theory without drag," *Astronomical Journal*, vol. 64, no. 1274, pp. 378–397, 1959.
- [27] R. A. Broucke, "The Effects of the J3-Harmonic (Pear Shape) on the Orbit of a Satellite," in *Predictability, Stability, and Chaos in N-Body Dynamical Systems*, A. E. Roy, Ed. New York: Plenum Press, 1991.
- [28] ———, "Long-term third-body effects via double averaging," *Journal of Guidance, Control, and Dynamics*, vol. 26, no. 1, pp. 27–32, 2003.
- [29] T. Guffanti and S. D'Amico, "Linear models for spacecraft relative motion perturbed by solar radiation pressure," *Journal of Guidance, Control, and Dynamics*, pp. 1–20, 2019.
- [30] T. Delabie, J. de Schutter, and B. Vandenbussche, "An Accurate and Efficient Gaussian Fit Centroiding Algorithm for Star Trackers," *Journal of the Astronautical Sciences*, vol. 61, no. 1, pp. 60–84, 2014.
- [31] D. Mortari, M. A. Samaan, C. Bruccoleri, and J. L. Junkins, "The pyramid star identification technique," *Navigation*, vol. 51, no. 3, pp. 171–183, 2004.
- [32] J. R. Wertz, *Spacecraft Attitude Determination and Control*. Springer Science & Business Media, 2012.
- [33] D. Reid, "An Algorithm for Tracking Multiple Targets," *IEEE Transactions on Automatic Control*, vol. 24, no. 6, pp. 843–854, 1979.
- [34] M. Chernick and S. D'Amico, "New Closed-Form Solutions for Optimal Impulsive Control of Spacecraft Relative Motion," *Journal of Guidance, Control, and Dynamics*, vol. 41, no. 2, pp. 301–319, 2018.
- [35] N. Stacey and S. D'Amico, "Adaptive and dynamically constrained process noise estimation for orbit determination," in *2019 AAS/AIAA Astrodynamics Specialist Conference*, Portland, Maine, 2019.
- [36] Y. Hu, I. Sharf, and L. Chen, "Three-spacecraft autonomous orbit determination and observability analysis with inertial angles-only measurements," *Acta Astronautica*, vol. 170, pp. 106–121, 2020.
- [37] S. Palo, G. Stafford, and A. Hoskins, "An Agile Multi-Use Nano Star Camera for Constellation Applications," in *27th Annual AIAA/USU Conference on Small Satellites*, Logan, Utah, 2013.
- [38] F. G. Lemoine, S. Goossens, T. J. Sabaka, J. B. Nicholas, E. Mazarico, D. D. Rowlands, B. D. Loomis, D. S. Chinn, G. A. Neumann, D. E. Smith, and M. T. Zuber, "Grm900c: A degree 900 lunar gravity model from grail primary and extended mission data." *Geophysical research letters*, vol. 41, no. 10, pp. 3382–3389, 2014.
- [39] S. K. Singh, R. Woollands, E. Taheri, and J. Junkins, "Feasibility of quasi-frozen, near-polar and extremely low-altitude lunar orbits," *Acta Astronautica*, vol. 166, pp. 450–468, 2020.

- [40] L. McManus and H. Schaub, "Establishing a formation of small satellites in a lunar flower constellation," *Advances in the Astronautical Sciences*, vol. 63, pp. 263–286, 2016.
- [41] R. L. Cognion, "Large phase angle observations of GEO satellites," in *Sensors and Systems for Space Applications VI*, K. D. Pham, J. L. Cox, R. T. Howard, and G. Chen, Eds., vol. 8739, International Society for Optics and Photonics. SPIE, 2013, pp. 194–205.
- [42] L. Galleani, L. Sacerdote, P. Tavella, and C. Zucca, "A mathematical model for the atomic clock error," *Metrologia*, vol. 40, pp. 257–264, 2003.
- [43] P. Cash, W. Krzewick, P. Machado, K. R. Overstreet, M. Silveira, M. Stanczyk, D. Taylor, and X. Zhang, "Microsemi Chip Scale Atomic Clock (CSAC) technical status, applications, and future plans," in *2018 European Frequency and Time Forum (EFTF)*, Turin, Italy, 2018, pp. 65–71.
- [44] C. Beierle and S. D'Amico, "Variable magnification optical stimulator for training and validation of spaceborne vision-based navigation," *Journal of Spacecraft and Rockets*, vol. 56, no. 4, 2019.